Structure

Article

Structural mechanism of TRPV5 inhibition by econazole

Graphical abstract

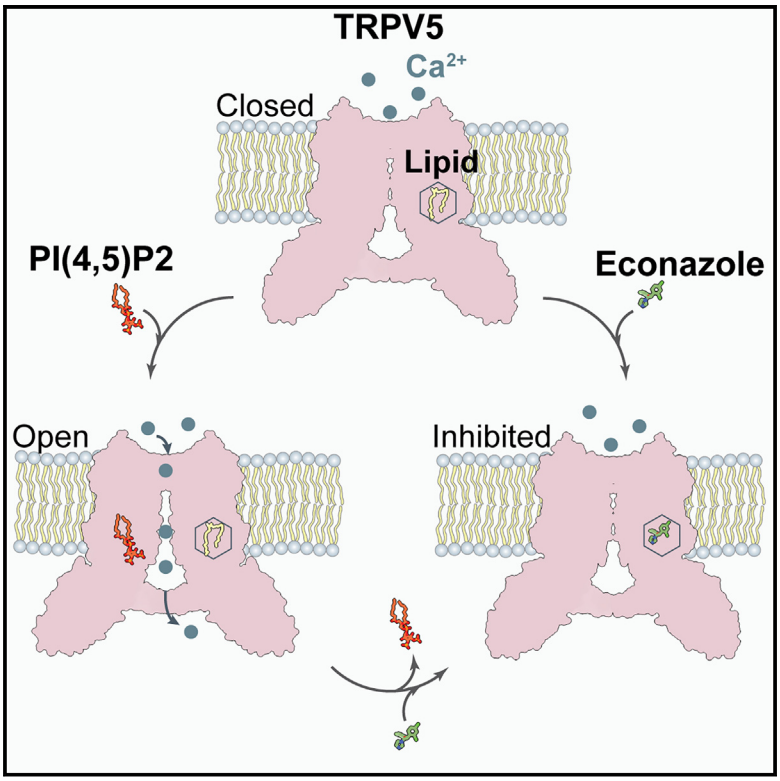

Highlights

- The cryo-EM structure of the TRPV5 in complex with the econazole was determined
- Residues F472, L475, and W495 form the econazole-binding site
- TRPV5 is inhibited through an inhibitor-activator competition mechanism

Authors

José J. De Jesús-Pérez, Matthew Gabrielle, Sumiyya Raheem, Edwin C. Fluck, Tibor Rohacs, Vera Y. Moiseenkova-Bell

Correspondence

vmb@pennmedicine.upenn.edu

In brief

De Jesús-Pérez et al. investigate the inhibitory mechanism of TRPV5 by the antifungal agent econazole. Combining cryo-EM, functional, and computational studies, they identified the binding site of the econazole. Mechanistically, their findings suggest that the econazole impedes the opening of the TRPV5 channel by PI(4,5)P_2, thereby resulting in its inhibition.

De Jesús-Pérez et al., 2024, Structure *32*, 148–156
February 1, 2024
https://doi.org/10.1016/j.str.2023.11.012

CellPress

CellPress

Structure

Article

Structural mechanism of TRPV5 inhibition by econazole

José J. De Jesús-Pérez,[1] Matthew Gabrielle,[2] Sumiyya Raheem,[2] Edwin C. Fluck,[1] Tibor Rohacs,[2] and Vera Y. Moiseenkova-Bell[1,3,*]

[1]Department of Systems Pharmacology and Translational Therapeutics, Perelman School of Medicine, University of Pennsylvania, Philadelphia, PA 19104, USA

[2]Department of Pharmacology, Physiology and Neuroscience, New Jersey Medical School, Rutgers University, Newark, NJ 07103, USA

[3]Lead contact

*Correspondence: vmb@pennmedicine.upenn.edu

https://doi.org/10.1016/j.str.2023.11.012

SUMMARY

The calcium-selective TRPV5 channel activated by phosphatidylinositol 4,5-bisphosphate [$PI(4,5)P_2$] is involved in calcium homeostasis. Recently, cryoelectron microscopy (cryo-EM) provided molecular details of TRPV5 modulation by exogenous and endogenous molecules. However, the details of TRPV5 inhibition by the antifungal agent econazole (ECN) remain elusive due to the low resolution of the currently available structure. In this study, we employ cryo-EM to comprehensively examine how the ECN inhibits TRPV5. By combining our structural findings with site-directed mutagenesis, calcium measurements, electrophysiology, and molecular dynamics simulations, we determined that residues F472 and L475 on the S4 helix, along with residue W495 on the S5 helix, collectively constitute the ECN-binding site. Additionally, the structure of TRPV5 in the presence of ECN and $PI(4,5)P_2$, which does not show the bound activator, reveals a potential inhibition mechanism in which ECN competes with $PI(4,5)P_2$, preventing the latter from binding, and ultimately pore closure.

INTRODUCTION

The transient receptor potential vanilloid type 5 (TRPV5), and its close relative (TRPV6), are highly calcium selective inwardly rectifying ion channels that demonstrate a remarkable preference for calcium (Ca^{2+}) over sodium by a factor of 100,[1,2] with an apparent affinity for Ca^{2+} of approximately 0.2 mM[3]. Physiologically, TRPV5 is expressed predominantly in the kidney, with lower levels detected in the placenta, testis, and osteoclasts.[3–8] In the kidney, TRPV5 is located on the apical surface of distal tubular epithelial cells and plays an important role in Ca^{2+} reabsorption.[9] Certain loss of function mutations in the human TRPV5 gene has been linked to the development of kidney stones,[10,11] whereas mice lacking this channel exhibit excessive calcium excretion in their urine, a condition known as hypercalciuria.[12]

Endogenously, TRPV5 is constitutively active and this activity depends on the plasma membrane phospholipid phosphatidylinositol-4,5-bisphosphate [$PI(4,5)P_2$].[13–15] On the other hand, TRPV5 is inhibited by low pH,[3,16–19] Mg^{2+},[2,13] as well as calcium-induced inactivation mediated by calmodulin binding to the inner base of the pore and the C terminus of the channel.[14,20,21] Additionally, this channel is inhibited by exogenous compounds such as econazole (ECN) (IC_{50} ~1.3–2 μM), miconazole (IC_{50} ~1.7 μM) ruthenium red (IC_{50} ~0.1 μM), ZINC9155420 (IC_{50} ~3 μM), and ZINC17988990 (IC_{50} ~0.1 μM).[22–24]

Originally, we determined the first cryoelectron microscopy (cryo-EM) structure of TRPV5 in complex with the antifungal ECN inhibitor at a resolution of 4.8 Å.[24] We proposed that the ECN-binding pocket is formed by F425 and I428 (S3 helix), L460 and C463 (S4 helix), I486 (S4-S5 linker), and I565 (S6 helix from the adjacent subunit), which corresponds to the canonical vanilloid-binding site in the TRPV1 channel.[25–27] This finding was supported by functional studies and site-directed mutagenesis, which demonstrated reduced inhibition with the F425A mutation. However, subsequent high-resolution TRPV5 structures in the absence of ECN revealed a similar density that resembles cholesterol.[14,15,21,28] Conversely, a recent cryo-EM structure of human TRPV6 (which shares 75% identity with TRPV5) in complex with ECN suggested a different binding site. In this case, the ECN is primarily stabilized by L475 and F472 of the S4 helix and W495 on the S5 helix.[29] Importantly, these residues are conserved in TRPV5 but only partially in the remaining TRPV channels. Those findings motivated us to re-examine our initially reported ECN-binding site in TRPV5.

Here, we present new cryo-EM structures of the TRPV5 channel in complex with ECN with or without the addition of $PI(4,5)P_2$ at resolutions of 2.86 and 2.94 Å, respectively. We identified a solid density between the S1, S4, and S5 helices in both structures that resembles the ECN density, similar to that observed in TRPV6.[29] Site-directed mutagenesis combined with electrophysiology, calcium measurements, and molecular dynamics

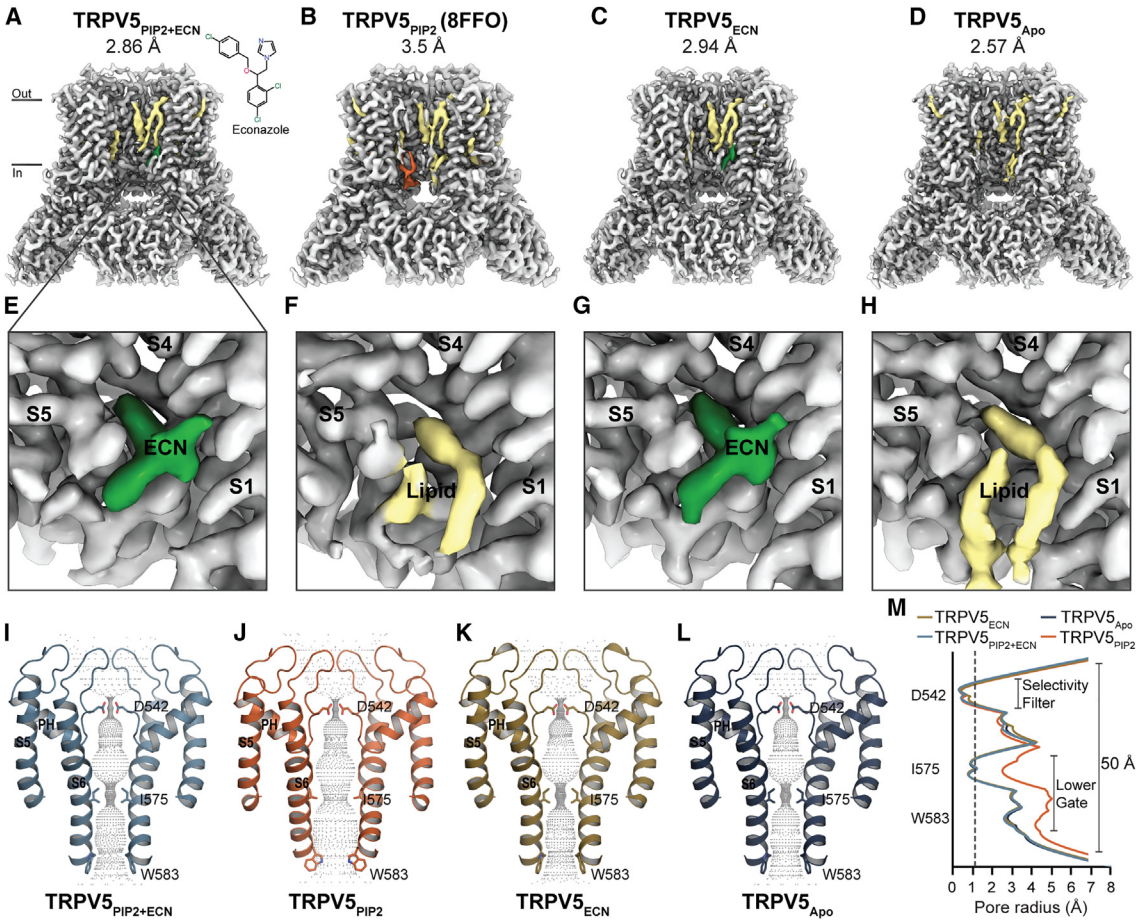

Figure 1. TRPV5 channel in complex with econazole in presence and absence of PI(4,5)P_2

Density maps and econazole (ECN)-binding site formed by S1, S4, and S5 helices of TRPV5 in the presence of PI(4,5)P_2 and ECN (A, E) and without ECN (PDB 8FFO) (B, F), and TRPV5 in the absence of PI(4,5)P_2 with (C, G) and without ECN (D, H). Insets in panel A depict the chemical structure of the ECN. Maps were contoured at 0.14 (A, B, C) and 0.16 (D) on chimeraX. For E–H, S1, S4, and S5 helices densities were selected using the respective coordinates model within the 2.5–3 Å range at same contour level than A–D, and splitted using *splitbyzone* chimera command. Horizontal gray lines delineate the membrane region. Lipids are represented in yellow, ECN in green, and PI(4,5)P_2 in orange. Hole generated-pore profile of $TRPV5_{PIP2+ECN}$ (I), $TRPV5_{PIP2}$ (J), $TRPV5_{ECN}$ (K), $TRPV5_{Apo}$ (L), and pore radii along the pathway (M). Dotted line at 1.1 Å signifies the radius of the dehydrated calcium ion. See also Figures S1–S3.

simulation confirmed that F472 and L475 residues on the S4 helix, along with W495 residue on the S5 helix, constitute the ECN-binding site in TRPV5. Furthermore, our structural analysis provides insights into the inhibition mechanism whereby ECN induces conformational changes in W495 and F493 on the S5 helix, leading to channel closure.

RESULTS

Structure of TRPV5 in complex with ECN

Our previous study of TRPV5 with ECN had TRPV5 stabilized in detergent and exposed to 6 μM ECN, which is approximately three times the IC_{50} value.[24] In contrast, its homologous structure, the human TRPV6, which remains open constitutively, was resolved in complex with ECN using nanodiscs, with a saturated concentration of 500 μM ECN.[29]

Based on these findings, we started with wild-type full-length rabbit TRPV5 purified and reconstituted into nanodiscs. We then prepared cryo-EM grids after incubating TRPV5 for 45 min with 400 μM of the channel activator PI(4,5)P_2 and 500 μM ECN (referred to as $TRPV5_{PIP2+ECN}$). This dataset revealed a single state at a resolution of 2.86 Å with C4 symmetry and 3.18 Å without symmetry (Figure 1A; Table 1; Figures S1–S3). The $TRPV5_{PIP2+ECN}$ map revealed distinct solid densities corresponding to various lipids including ergosterol (ERG), the yeast analog to cholesterol, which had been previously observed in other TRPV5 structures[14,15,21,24,28] (Figures 1A–1D). We noticed that the ECN-binding pocket we previously reported[24] was occupied by an ERG molecule in our new preparation (Figure S3). Notably, we also observed a robust extra density between the S1 helix, the S4 helix, and the S5 helix from the adjacent subunit, with geometry consistent with the ECN molecule (Figures 1E and 2A). This finding parallels the observation made in human TRPV6;[29] however, in that structure, an additional elongated density is also observed in the binding pocket (Figure S4). Notably, we did not detect the canonical PI(4,5)P_2 density in the $TRPV5_{PIP2+ECN}$ map (Figure S3).

Table 1. Cryo-EM data collection and model statistics

	$TRPV5_{ECN}$ (EMD-41218, PDB 8TF3)	$TRPV5_{PIP2+ECN}$ (EMD-41219, PDB 8TF4)	$TRPV5_{Apo}$ (EMD-41217, PDB 8TF2)
Data collection and processing			
Magnification	105,000x	105,000x	105,000x
Voltage (kV)	300	300	300
Camera	K3	K3	K3
Defocus range (μm)	−0.8 to −2.5	−0.8 to −2.5	−0.8 to −2.5
Pixel size (Å)	0.83	0.83	0.83
Micrographs	6,018	11,346	6,049
Particles from 2D classification (no.)	324,769	306,512	704,782
Final particles (no.)	173,323	101,063	79,632
Symmetry	C4	C4	C4
Map resolution (Å)	2.94	2.86	2.57
FSC threshold	0.143	0.143	0.143
Model refinement			
Model composition			
Nonhydrogen atoms	19,888	19,888	19,856
Protein residues	2,408	2,408	2,408
Ligands	20	20	24
R.M.S. deviations			
Bond lengths (Å)	0.028	0.028	0.028
Bond angles (°)	2.403	2.376	2.369
Validation			
MolProbity score	1.35	1.29	1.22
Clashscore	4.45	5.28	4.43
Rotamer outliers (%)	0.00	0.58	0.38
Ramachandran plot			
Favored (%)	97.32	97.99	98.49
Allowed (%)	2.68	2.01	1.51
Disallowed (%)	0.00	0.00	0.00

Deposition codes, data collection, processing, and model refinement.

As a control, we prepared grids of TRPV5 with 400 μM $PI(4,5)P_2$ ($TRPV5_{PIP2}$) without ECN.[30] The resulting map displayed an open-state structure at a resolution of 3.5 Å (Figures 1B, 1J, and 1K), with a well-defined density at the previously described $PI(4,5)P_2$-binding site (Figures S3C and S3D). Similar to the $TRPV5_{PIP2+ECN}$ map, the $TRPV5_{PIP2}$ exhibited an ERG molecule within the vanilloid pocket (Figure S3) and lipid tails occupying the site where the ECN density was observed in the $TRPV5_{PIP2+ECN}$ structure (Figure 1F).

Next, we investigated whether ECN can bind to TRPV5 in the absence of $PI(4,5)P_2$, as in our previous study.[24] We prepared grids of TRPV5 incubated with 500 μM ECN for 45 min ($TRPV5_{ECN}$). The resulting dataset yielded a single state at 2.94 Å resolution with C4 symmetry and 3.25 Å without symmetry (Figures 1C, S2, and S3). As in the $TRPV5_{PIP2+ECN}$ structure, $TRPV5_{ECN}$ showed an ERG molecule within the canonical vanilloid pocket (Figure S3) and solid ECN density between the S1, S4, and S5 helices (Figures 1G and 2B). As a control for this condition, we prepared grids of TRPV5 without any treatment ($TRPV5_{Apo}$). The resulting structure also showed a single closed state at resolution of 2.57 Å with C4 symmetry as it has already been published.[14,15,21] Most importantly, lipids and ERG molecules were solved at the same position as $TRPV5_{ECN}$ and $TRPV5_{PIP2+ECN}$ structures; specially, lipid tails occupy the pocket made by the S2, S4, and S5 helices (Figure 1H). These results confirmed that TRPV5 could bind ECN in the apo state and remains in the same conformational state (Figures 1D and 1H).

The ECN-binding site

In comparison to $TRPV5_{Apo}$, $TRPV5_{ECN}$ (root-mean-square deviation [RMSD] = 0.19 Å) and $TRPV5_{PIP2+ECN}$ (RMSD = 0.18 Å) adopt the same closed conformational state (Figures 1I–1M). Likewise, we found that the occupation of the ECN-binding site by the antifungal compound is indistinguishable between the states of the channel (Figures 2A and 2B). In both the $TRPV5_{ECN}$ and the $TRPV5_{PIP2+ECN}$ structures, the imidazole group of the ECN maintains a CH/π interaction[31–33] between the W495 on the S5 helix (at a distance of ∼3.6 Å) and the F472 on the C terminus of the S4 helix (at ∼3.8 Å), as well as with L475 at a distance of 3.1 Å (Figure S4); the chlorophenyl group is also underpinned by a CH/π interaction with the V465 on the S4 helix and L475 (at ∼3.5 Å) on the S4-S5 linker, along with L496 (at ∼2.6 Å) and V499 (at ∼3.7 Å) on the S5 helix; and the dichlorophenyl group could interact with S334 (at ∼3.4 Å) and I337 (at ∼4.1 Å) on the S1 helix (Figures 2A and 2B). Similar results were observed in the TRPV6 structure;[29] however, in this case, the dichlorophenyl group is sandwiched between W495 of S5 and F472 of S4 (Figure S4). Surprisingly, the ECN-binding pocket seems to be a permanent cavity and needs to be filled, as observed in the $TRPV5_{PIP2}$ and $TRPV5_{Apo}$ structures where it is occupied by lipid tails (Figure 2C).

Inhibition mechanism of TRPV5 by ECN

To establish the molecular mechanism underlying the closure of the TRPV5 channel caused by ECN, we compared the $PI(4,5)P_2$-activated TRPV5 and $TRPV5_{PIP2+ECN}$ structures. As previously reported, the $TRPV5_{PIP2}$ structure revealed that $PI(4,5)P_2$ binds to the basic residue network formed by R302, R305, K484, and R584, where the interaction with R584 causes the S6 helix to be pulled out of the pore[14,15,30] (Figure S3E). This action widens the pore at I575, where the lower gate is located (Figure 1J). In the presence of ECN, this process is reversed. Once ECN occupies the binding site, it induces a 16.6° rotation of W495 toward the ECN pocket (Figure 3A) and a 13.9° downward rotation (Figure 3B). This movement, in turn, leads to an 8.8° inward rotation of the S5 helix toward the center of the pore (Figure 3B). Consequently, the F493 residue on the S5 helix undergoes a 31° rotation (Figure 3A) and sterically interacts with the pore helix (S6) at F574. This interaction pushes the S6 helix toward the center of the pore by 9.4° (Figure 3B), decreasing the pore radius from ∼3.0 to ∼1.0 Å at I575 and from ∼4.2 to ∼2.5 Å at W583 (Figure 1M). In the meantime, W583 and R584 undergo a rotation of ∼114° and 63° toward the pore, respectively (Figure 3D). This rearrangement disrupts the salt bridge between R584 and $PI(4,5)P_2$, and the channel closes. During this process, the F478 residue on the S4-S5 linker from the adjacent subunit undergoes a

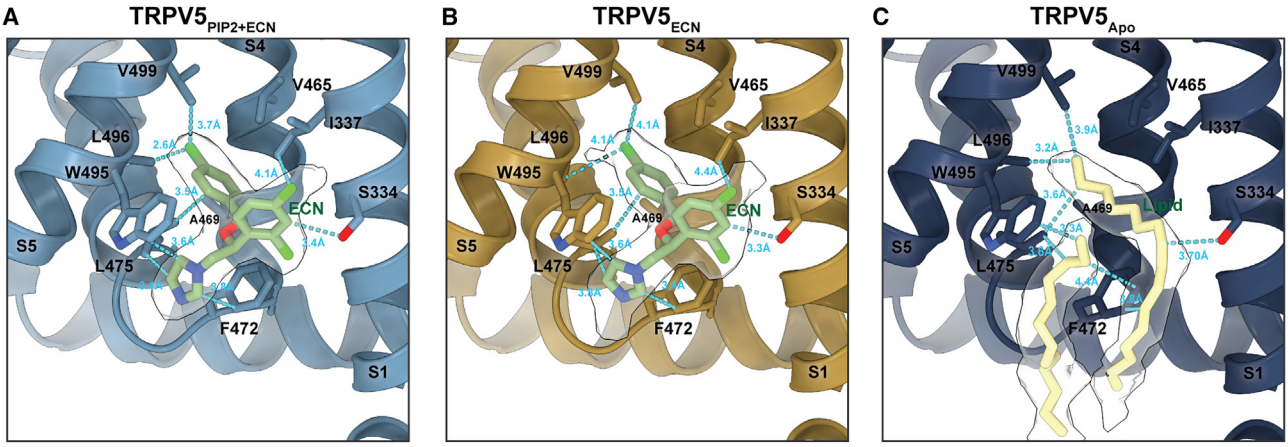

Figure 2. Econazole-binding site of TRPV5

Econazole-protein interactions determine using LigPlot in $TRPV5_{PIP2+ECN}$ (A), $TRPV5_{ECN}$ (B), and the lipid tails in $TRPV5_{Apo}$ (C), with overlaid transparent density contoured at the same contour level than Figure 1 ($\sigma = 3$). Map densities were splitted as was described in Figure 1. Dotted blue lines connect two atoms used to calculate the distance (blue). See also Figures S3–S5.

101.2° upward rotation to occupy the space left by F493 and L573 (Figure 3C). Simultaneously, this movement creates enough space for the R492 residue, which is situated at a distance of ~5.2 Å from F478, to adjust its position also in response to changes in the S5 helix (Figure 3C). As the channel transition into its inhibited state, R492 moves closer to F478 (at ~5.5 Å). Interestingly, this closer proximity to F478 coincides with R492 moving farther away from the 4′-phosphate of the $PI(4,5)P_2$, shifting from its original distance of ~4.9 to ~7.7 Å (Figure 3D). This observation suggests a potential connection between the $PI(4,5)P_2$ and the ECN-binding sites.

Remarkably, those conformational changes are not exclusive to TRPV5; the human TRPV6 inhibited by ECN exhibits similar rotations of W495, F493, and F478 residues even though the dichlorophenyl from the ECN is the group that interacts with the F472 and W495 (Figure S4B). However, the TRPV6 channel undergoes an α-to-π transition in the S6 helix during this process, which has been seen in any TRPV5 structure.[14,15,21,23,24]

F472, L475, and W495 constitute the ECN-binding site

In order to corroborate the ECN-binding site of TRPV5, we transfected HEK293 cells with wild-type, F472A, L475A, or W495A TRPV5 and performed intracellular Ca^{2+} concentration measurements and whole-cell patch clamp experiments to assess their sensitivity to ECN inhibition. The W495A mutant was not functional, indicating that this residue plays a crucial rule in the functioning of the channel, thus we focused on testing ECN sensitivity of the F472A and L475A mutants. First, we performed intracellular Ca^{2+} measurements to detect Ca^{2+} influx through the channels (Figures S5A–S5D). The wild-type TRPV5 exhibited an IC_{50} value of 13 ± 2 μM (n = 3). However, the inhibitory effect was diminished in the F472A mutant, which displayed an IC_{50} value of 44 ± 12 μM (n = 3). The impact was even greater in the L475A mutant, which exhibited an IC_{50} value of 125 ± 8 μM (n = 3) (Figure 4A). Unfortunately, the low solubility of ECN prevented us from reaching full inhibition, especially in the mutant channels, introducing some uncertainty to the IC_{50} values. Thus, we confirmed reduced ECN inhibition of the mutant channels by measuring monovalent currents through TRPV5 in whole-cell patch clamp experiments (Figures S5E–S5G). Monovalent currents were inhibited by ~100% (n = 7) in wild-type TRPV5, but only by ~65% (n = 6) in the F472A mutant and ~25% (n = 6) in the L475A mutant when exposed to 10 μM ECN (Figure 4B). We also tested the double-mutant F472A-L475A, and charge L475 mutants; however, all of them were not functional (Figure S5).

Next, to further validate the role of these residues in ECN binding, we conducted a 500 ns all-atom molecular dynamics simulation starting with $TRPV5_{PIP2+ECN}$. Through RMSD, we observed that the protein achieved a stable configuration along the simulation with an RMSD value ranging from 2.5 to 3.0 Å (Figure S5E). Similarly, the root-mean-square fluctuation analysis revealed that the ECN-binding residues exhibited fluctuations of approximately 1.2 Å (Figure S5I). Additionally, the ECN molecules displayed RMSDs ranging from 1.0 to 3.0 Å, however, also show a wide range of movement (Figures 4D and S5E–S5H). This enhanced mobility could be attributed to their location at the interface between the membrane, water, and the protein, where they experience dynamic interactions. We further examined the nonbonded interactions by measuring the distance between each residue forming the binding site and the center of the mass of the ligand, revealing that the ECN primarily interacts with the A333, I337, A469, F472, L475, and W495 residues (Figure 4E, top). Consistently, the decomposition analysis of the binding energy indicated that I337, F472, L475, and W495 contribute significantly to the overall binding energy (Figure 4E, bottom).

In summary, our data suggest that the F472, L475, and W495 residues make important contributions to the ECN-binding site, which remains conserved in both TRPV5 and TRPV6 channels.

DISCUSSION

In our previous ECN-bound TRPV5 structure solubilized in detergent, we proposed that the ECN binds to the canonical vanilloid-binding site;[24,26] however, recent structures at higher resolution in the absence of the ECN contain similar elongated densities

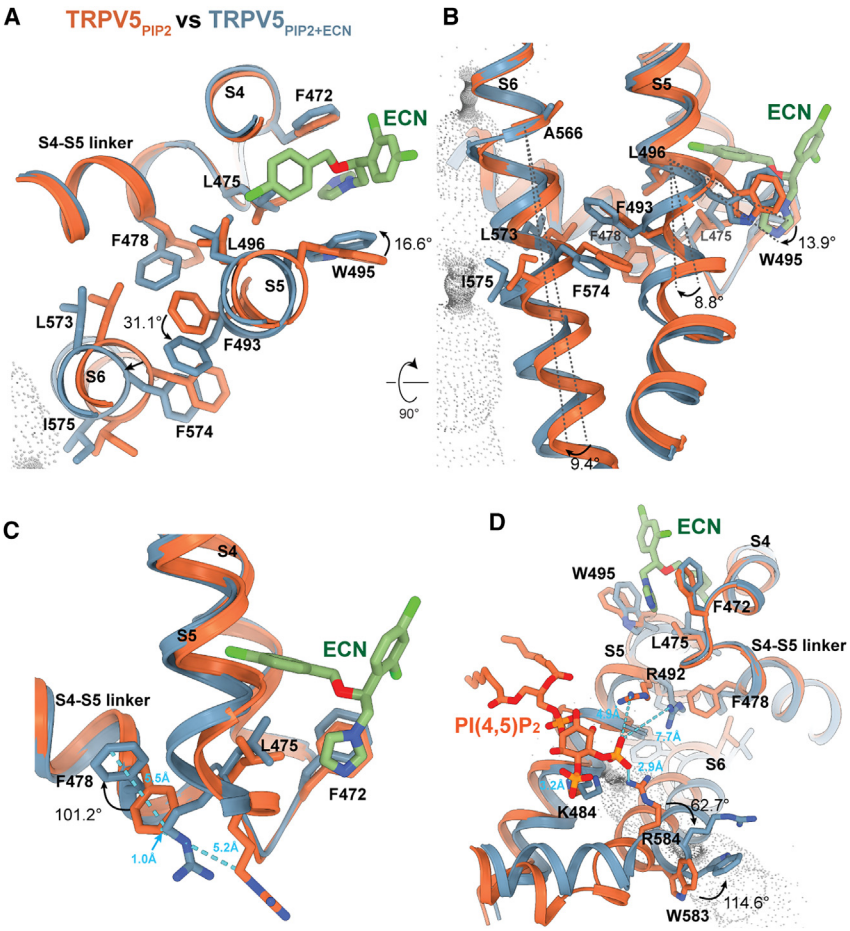

Figure 3. Conformational changes of TRPV5 inhibited by econazole

Comparative structural analysis of the TRPV5 activated with PI(4,5)P_2 (orange) and inhibited by ECN (blue): view from extracellular (A), parallel to the membrane (B, C), and from intracellular side (D) of S4, S4-S5 linker, S5, and S6 helices. The pore region is represented by gray dots. Structural rotation and displacements are indicated by curved and straight arrows, respectively. Blue dash lines link atoms employed for distance calculation. See also Figure S4.

at the vanilloid pocket that resemble a cholesterol molecule.[14,15,21,28] Despite the functional studies that we showed to support our conclusions, certain factors such as the low concentration of the inhibitor used in the preparation, the use of detergent instead of nanodiscs, and the low resolution of the resulting map may have impacted determination of the true ECN-binding site.

In this new study, we solved the structure of TRPV5 in complex with the inhibitor ECN, both in the presence and absence of the activator PI(4,5)P_2, at much higher resolution. Our findings demonstrate that TRPV5 and TRPV6 share a conserved ECN-binding site. Specifically, in TRPV5, ECN is primarily stabilized by CH/π interactions with F472 on the S4 helix, L475 on the S4-S5 linker, and the W495 residue on the S5 helix (Figure S4). Moreover, we observed that the density presented in the canonical vanilloid site resembles an ERG molecule, which may function as the structural lipid that has also been seen in TRPV6.[34] Notably, the F425 residue that we previously reported as part of the ECN-binding site is in contact with the S4 helix at Y467 (Figure S4G).[24] This could explain the reduction in ECN inhibition observed in our earlier studies.

Interestingly, when ECN was applied to PI(4,5)P_2-activated TRPV5, it prevented PI(4,5)P_2 from binding to the channel, consistent with the expected behavior of an inactive channel. Similar results were obtained when TRPV5 was simultaneously exposed to PI(4,5)P_2 and the ruthenium red (RR) blocker (J.J.d.J.-P. and V.Y.M.-B., unpublished data) or low pH.[15] In the case of RR, it was found that RR binds to the pore above the lower gate, interacts with N572, and causes the closure of the pore by disrupting the R584-PI(4,5)P_2 interaction (J.J.d.J.-P. and V.Y.M.-B., unpublished data). On the other hand, Fluck et al. propose that the inhibition of TRPV5 at low pH is a result of salt bridge formation around K607 (the intracellular pH sensor) and the interruption of PI(4,5)P_2 interaction with the channel.

These mechanisms partially align with our current findings. Our proposed model suggests that ECN initiates pore closure in TRPV5 by interacting via CH/π interactions with W495 on the S5 helix and F472. This contact facilitates the movement of the S5 helix and the rotation of F493 residue to interact sterically with the S6 helix at F574. Thus, the S6 helix is driven toward the pore, resulting in its closure. The reduction of the pore size at the lower gate promotes the rotation of the W583 residue toward the pore (Figure 1M), leading to the loss of the salt bridge between the 4′-phosphate of the PI(4,5)P_2 and the R584 residues. Furthermore, the movement of the S5 helix substantially increases the distance between R492 and the 4′-phosphate of PI(4,5)P_2. Although in our case that distance is ~4.7 Å (TRPV5$_{PIP2}$), it has been reported that it can be reduced to approximately 3.6 Å (7T6Q),[15] with a ~0.5 of probability of interaction based on molecular dynamics simulation.[35] While these disrupted interactions could potentially perturb the interaction of PI(4,5)P_2 with R302, R305, and K484, experiments involving R584 mutations have shown only modest decreases in channel activation by PI(4,5)P_2,[36] suggesting there may also be an allosteric influence on TRPV5 inhibition by ECN.

The conformational changes resulting from the movement of F493 and the S6 helix at F574 create an empty space that is refilled by F478. This triangular zone of phenylalanines appears to be crucial for channel function. Functional studies focusing on the vicinity of the lower gate (I575) have shown that mutation of M577 to asparagine in rat TRPV5 (located at 3.6 Å from F478 in the TRPV5$_{PIP2}$, Figure S4H) or in human TRPV6 (M517N, at 3.5 Å from F478 in the TRPV5$_{open}$) produces an increase in the Ca^{2+} currents.[37] Furthermore, F493 is conserved in all TRPV

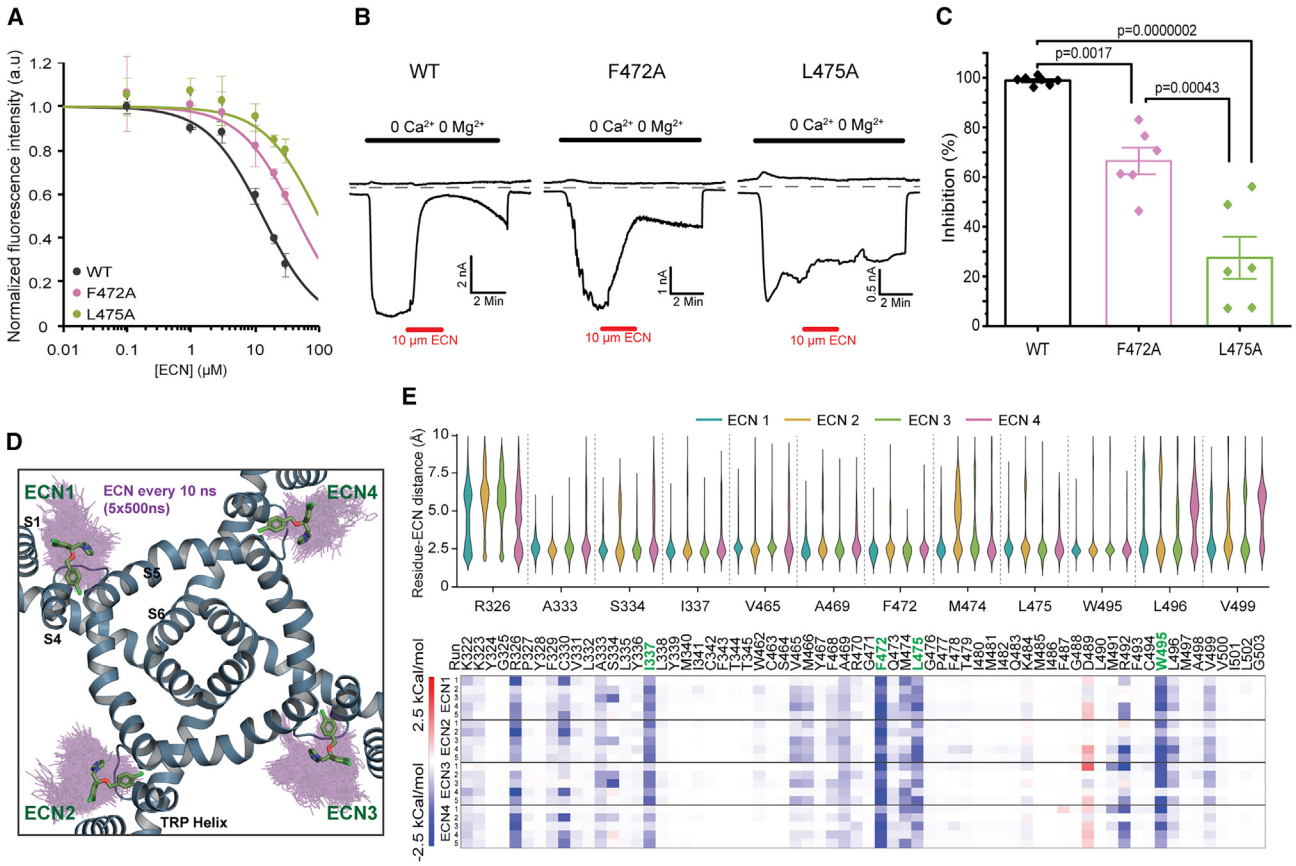

Figure 4. TRPV5 inhibition by econazole

(A) Intracellular Ca^{2+} concentration measurements were performed in HEK293 cells transfected with the Ca^{2+} sensor GCaMP6 and wild-type or mutant rbTRPV5 channels, as described in the STAR methods section. Cells were pretreated with various concentrations of econazole in a Ca^{2+}-free extracellular solution, and the increases of fluorescence in response to increasing extracellular Ca^{2+} to 1 mM were plotted, normalized to the response evoked in cells without econazole pretreatment, n = 3 different transfections. See Figure S5 for representative traces and further details. All data plotted as mean ± SEM.

(B) Representative currents from HEK293 cells transfected with wild-type or mutant rbTRPV5. Whole-cell patch clamp experiments were performed as described in the Methods section. At the beginning of the experiment, the cells were kept in a nominally Ca^{2+}-free solution containing 1 mM Mg^{2+}. In this solution, currents are largely blocked by Mg^{2+} and the trace amounts of Ca^{2+}. Monovalent currents were initiated by removing Mg^{2+} and chelating Ca^{2+} with EGTA (0 Ca^{2+} 0 Mg^{2+}). Top traces show currents at 100 mV, bottom traces at −100 mV, the dashed line indicates zero current. The application of 10 μM econazole (ECN) is indicated by the horizontal lines. (C) The percent inhibition evoked by 10 μM econazole is plotted. Statistical significance was calculated with one-way analysis of variance and Tukey's post hoc test. The bar height is the mean ± SEM (D) Dynamic configuration of ECN molecules (purple) within each subunit (ECN1–ECN4) sampled at 10 ns intervals from every of the five independent replicas of 500 ns all-atom molecular dynamics simulation. These conformations are compared to the position observed in $TRPV_{PIP2+ECN}$ cryostructure (green). (E) Top, the violin plot showcases the distribution of distances from the center of mass of the ECN molecules within each of the 4 subunits (ECN1–ECN4) to the key residues constituting the binding site, compiled from the total 2.5 μs simulation (5 × 500 ns): bottom, a heatmap representation of mean binding energies per residue, calculated at 10 ns intervals across each of the five simulations (denoted as 1–5) and for each ECN molecule (ECN1–ECN4) employing the g_mmpbsa tool and the solvent-accessible surface are (SASA) model. Residues that contribute most significantly to the binding energy are depicted in green. See also Figures S5.

subfamily members, while F478 is replaced by a tyrosine in TRPV1-4 channels (Figure S5), indicating that these residues could play a significant role in the TRPV channel function.

In summary, our molecular findings provide insights into the binding and inhibitory mechanism of ECN on the TRPV5 channel. These results help us for the development of new pharmacological tools to regulate Ca^{2+}-selective TRPV subfamily channels.

STAR★METHODS

Detailed methods are provided in the online version of this paper and include the following:

- KEY RESOURCES TABLE
- RESOURCE AVAILABILITY
  - Lead contact
  - Materials availability
  - Data and code availability
- EXPERIMENTAL MODEL AND STUDY PARTICIPANT DETAILS
- METHOD DETAILS
  - TRPV5 protein preparation
  - Cryo-EM sample preparation and data collection
  - Data processing
  - Model building

- Molecular dynamics simulations
- Whole-cell patch clamp
- Intracellular Ca^{2+} measurements

● QUANTIFICATION AND STATISTICAL ANALYSIS

SUPPLEMENTAL INFORMATION

Supplemental information can be found online at https://doi.org/10.1016/j.str.2023.11.012.

ACKNOWLEDGMENTS

We acknowledge the use of instruments at the Electron Microscopy Resource Lab and at the Beckman Center for Cryo-Electron Microscopy at the University of Pennsylvania Perelman School of Medicine. We also thank Stefan Steimle for assistance with Krios microscope operation at the University of Pennsylvania. We thank Ruth A. Pumroy for critical manuscript reading and advice throughout the project. This work was supported by grants from the National Institutes of Health (R35GM144120 to V.Y.M.-B. and R01GM093290 to T.R.).

AUTHOR CONTRIBUTIONS

Conceptualization, J.J.d.J.-P. and V.Y.M.-B.; methodology, J.J.d.J.-P., M.G., and S.R.; validation, J.J.d.J.-P., M.G., S.R., and E.C.F.; formal analysis, J.J.d.J.-P., M.G., S.R., and E.C.F.; investigation, J.J.d.J.-P., M.G., S.R., and E.C.F.; visualization, J.J.d.J.-P., M.G., and S.R.; supervision, T.R. and V.Y.M.-B.; funding acquisition, T.R. and V.Y.M.-B.; writing – original draft, J.J.d.J.-P., T.R., and V.Y.M.-B.; writing – review and editing, J.J.d.J.-P., T.R., and V.Y.M.-B.

DECLARATION OF INTERESTS

The authors declare that they have no competing interests.

Received: August 3, 2023
Revised: November 1, 2023
Accepted: November 28, 2023
Published: December 22, 2023

REFERENCES

1. Vennekens, R., Hoenderop, J.G., Prenen, J., Stuiver, M., Willems, P.H., Droogmans, G., Nilius, B., and Bindels, R.J. (2000). Permeation and gating properties of the novel epithelial Ca(2+) channel. J. Biol. Chem. *275*, 3963–3969.
2. Nilius, B., Vennekens, R., Prenen, J., Hoenderop, J.G., Droogmans, G., and Bindels, R.J. (2001). The single pore residue Asp542 determines Ca2+ permeation and Mg2+ block of the epithelial Ca2+ channel. J. Biol. Chem. *276*, 1020–1025.
3. Hoenderop, J.G., van der Kemp, A.W., Hartog, A., van de Graaf, S.F., van Os, C.H., Willems, P.H., and Bindels, R.J. (1999). Molecular identification of the apical Ca2+ channel in 1, 25-dihydroxyvitamin D3-responsive epithelia. J. Biol. Chem. *274*, 8375–8378.
4. Müller, D., Hoenderop, J.G., Meij, I.C., van den Heuvel, L.P., Knoers, N.V., den Hollander, A.I., Eggert, P., García-Nieto, V., Claverie-Martín, F., and Bindels, R.J. (2000). Molecular cloning, tissue distribution, and chromosomal mapping of the human epithelial Ca2+ channel (ECAC1). Genomics *67*, 48–53.
5. van der Eerden, B.C.J., Hoenderop, J.G.J., de Vries, T.J., Schoenmaker, T., Buurman, C.J., Uitterlinden, A.G., Pols, H.A.P., Bindels, R.J.M., and van Leeuwen, J.P.T.M. (2005). The epithelial Ca2+ channel TRPV5 is essential for proper osteoclastic bone resorption. Proc. Natl. Acad. Sci. USA *102*, 17507–17512.
6. Bernucci, L., Henríquez, M., Díaz, P., and Riquelme, G. (2006). Diverse calcium channel types are present in the human placental syncytiotrophoblast basal membrane. Placenta *27*, 1082–1095.
7. Li, S., Wang, X., Ye, H., Gao, W., Pu, X., and Yang, Z. (2010). Distribution profiles of transient receptor potential melastatin- and vanilloid-related channels in rat spermatogenic cells and sperm. Mol. Biol. Rep. *37*, 1287–1293.
8. Jang, Y., Lee, Y., Kim, S.M., Yang, Y.D., Jung, J., and Oh, U. (2012). Quantitative analysis of TRP channel genes in mouse organs. Arch Pharm. Res. (Seoul) *35*, 1823–1830.
9. Hoenderop, J.G.J., Nilius, B., and Bindels, R.J.M. (2005). Calcium absorption across epithelia. Physiol. Rev. *85*, 373–422.
10. Oddsson, A., Sulem, P., Helgason, H., Edvardsson, V.O., Thorleifsson, G., Sveinbjörnsson, G., Haraldsdottir, E., Eyjolfsson, G.I., Sigurdardottir, O., Olafsson, I., et al. (2015). Common and rare variants associated with kidney stones and biochemical traits. Nat. Commun. *6*, 7975.
11. Wang, L., Holmes, R.P., and Peng, J.B. (2017). The L530R variation associated with recurrent kidney stones impairs the structure and function of TRPV5. Biochem. Biophys. Res. Commun. *492*, 362–367.
12. Hoenderop, J.G.J., van Leeuwen, J.P.T.M., van der Eerden, B.C.J., Kersten, F.F.J., van der Kemp, A.W.C.M., Mérillat, A.M., Waarsing, J.H., Rossier, B.C., Vallon, V., Hummler, E., and Bindels, R.J.M. (2003). Renal Ca2+ wasting, hyperabsorption, and reduced bone thickness in mice lacking TRPV5. J. Clin. Invest. *112*, 1906–1914.
13. Lee, J., Cha, S.K., Sun, T.J., and Huang, C.L. (2005). PIP2 activates TRPV5 and releases its inhibition by intracellular Mg2+. J. Gen. Physiol. *126*, 439–451.
14. Hughes, T.E.T., Pumroy, R.A., Yazici, A.T., Kasimova, M.A., Fluck, E.C., Huynh, K.W., Samanta, A., Molugu, S.K., Zhou, Z.H., Carnevale, V., et al. (2018). Structural insights on TRPV5 gating by endogenous modulators. Nat. Commun. *9*, 4198.
15. Fluck, E.C., Yazici, A.T., Rohacs, T., and Moiseenkova-Bell, V.Y. (2022). Structural basis of TRPV5 regulation by physiological and pathophysiological modulators. Cell Rep. *39*, 110737.
16. Vennekens, R., Prenen, J., Hoenderop, J.G., Bindels, R.J., Droogmans, G., and Nilius, B. (2001). Modulation of the epithelial Ca2+ channel ECaC by extracellular pH. Pflugers Arch. *442*, 237–242.
17. Cha, S.K., Jabbar, W., Xie, J., and Huang, C.L. (2007). Regulation of TRPV5 single-channel activity by intracellular pH. J. Membr. Biol. *220*, 79–85.
18. Yeh, B.I., Kim, Y.K., Jabbar, W., and Huang, C.L. (2005). Conformational changes of pore helix coupled to gating of TRPV5 by protons. EMBO J. *24*, 3224–3234.
19. Yeh, B.I., Sun, T.J., Lee, J.Z., Chen, H.H., and Huang, C.L. (2003). Mechanism and molecular determinant for regulation of rabbit transient receptor potential type 5 (TRPV5) channel by extracellular pH. J. Biol. Chem. *278*, 51044–51052.
20. de Groot, T., Kovalevskaya, N.V., Verkaart, S., Schilderink, N., Felici, M., van der Hagen, E.A.E., Bindels, R.J.M., Vuister, G.W., and Hoenderop, J.G. (2011). Molecular mechanisms of calmodulin action on TRPV5 and modulation by parathyroid hormone. Mol. Cell Biol. *31*, 2845–2853.
21. Dang, S., van Goor, M.K., Asarnow, D., Wang, Y., Julius, D., Cheng, Y., and van der Wijst, J. (2019). Structural insight into TRPV5 channel function and modulation. Proc. Natl. Acad. Sci. USA *116*, 8869–8878.
22. Nilius, B., Prenen, J., Vennekens, R., Hoenderop, J.G., Bindels, R.J., and Droogmans, G. (2001). Pharmacological modulation of monovalent cation currents through the epithelial Ca2+ channel ECaC1. Br. J. Pharmacol. *134*, 453–462.
23. Hughes, T.E., Del Rosario, J.S., Kapoor, A., Yazici, A.T., Yudin, Y., Fluck, E.C., 3rd, Filizola, M., Rohacs, T., and Moiseenkova-Bell, V.Y. (2019). Structure-based characterization of novel TRPV5 inhibitors. Elife *8*, e49572.
24. Hughes, T.E.T., Lodowski, D.T., Huynh, K.W., Yazici, A., Del Rosario, J., Kapoor, A., Basak, S., Samanta, A., Han, X., Chakrapani, S., et al.

(2018). Structural basis of TRPV5 channel inhibition by econazole revealed by cryo-EM. Nat. Struct. Mol. Biol. *25*, 53–60.

25. Gao, Y., Cao, E., Julius, D., and Cheng, Y. (2016). TRPV1 structures in nanodiscs reveal mechanisms of ligand and lipid action. Nature *534*, 347–351.
26. Cao, E., Liao, M., Cheng, Y., and Julius, D. (2013). TRPV1 structures in distinct conformations reveal activation mechanisms. Nature *504*, 113–118.
27. Nadezhdin, K.D., Neuberger, A., Nikolaev, Y.A., Murphy, L.A., Gracheva, E.O., Bagriantsev, S.N., and Sobolevsky, A.I. (2021). Extracellular cap domain is an essential component of the TRPV1 gating mechanism. Nat. Commun. *12*, 2154.
28. Rohacs, T., Fluck, E.C., De Jesús-Pérez, J.J., and Moiseenkova-Bell, V.Y. (2022). What structures did, and did not, reveal about the function of the epithelial Ca(2+) channels TRPV5 and TRPV6. Cell Calcium *106*, 102620.
29. Neuberger, A., Nadezhdin, K.D., and Sobolevsky, A.I. (2021). Structural mechanisms of TRPV6 inhibition by ruthenium red and econazole. Nat. Commun. *12*, 6284.
30. Lee, B.H., De Jesús Pérez, J.J., Moiseenkova-Bell, V., and Rohacs, T. (2023). Structural basis of the activation of TRPV5 channels by long-chain acyl-Coenzyme-A. Nat. Commun. *14*, 5883.
31. Spiwok, V. (2017). CH/pi Interactions in Carbohydrate Recognition. Molecules *22*, 1038.
32. Takahashi Osamu, K.Y., Sachiyo, I., Saito, K., Michio, I., Tomoda, S., Umezawa, Y., Sei, T., and Motohiro, N. (2001). Hydrogen-Bond-Like Nature of the CH/π Interaction as Evidenced by Crystallographic Database Analyses and Ab Initio Molecular Orbital Calculations. Bull. Chem. Soc. Jpn. *74*, 9.
33. Nishio, M. (2011). The CH/pi hydrogen bond in chemistry. Conformation, supramolecules, optical resolution and interactions involving carbohydrates. Phys. Chem. Chem. Phys. *13*, 13873–13900.
34. Humer, C., Lindinger, S., Carrel, A.L., Romanin, C., and Höglinger, C. (2022). TRPV6 Regulation by Cis-22a and Cholesterol. Biomolecules *12*, 804.
35. Fathizadeh, A., Senning, E., and Elber, R. (2021). Impact of the Protonation State of Phosphatidylinositol 4,5-Bisphosphate (PIP2) on the Binding Kinetics and Thermodynamics to Transient Receptor Potential Vanilloid (TRPV5): A Milestoning Study. J. Phys. Chem. B *125*, 9547–9556.
36. Rohács, T., Lopes, C.M.B., Michailidis, I., and Logothetis, D.E. (2005). PI(4,5)P2 regulates the activation and desensitization of TRPM8 channels through the TRP domain. Nat. Neurosci. *8*, 626–634.
37. Zheng, W., Hu, R., Cai, R., Hofmann, L., Hu, Q., Fatehi, M., Long, W., Kong, T., Tang, J., Light, P., et al. (2018). Identification and characterization of hydrophobic gate residues in TRP channels. FASEB J *32*, 639–653.
38. Moiseenkova-Bell, V.Y., Stanciu, L.A., Serysheva, I.I., Tobe, B.J., and Wensel, T.G. (2008). Structure of TRPV1 channel revealed by electron cryomicroscopy. Proc. Natl. Acad. Sci. USA *105*, 7451–7455.
39. Grinkova, Y.V., Denisov, I.G., and Sligar, S.G. (2010). Engineering extended membrane scaffold proteins for self-assembly of soluble nanoscale lipid bilayers. Protein Eng. Des. Sel. *23*, 843–848.
40. Punjani, A., and Fleet, D.J. (2021). 3D variability analysis: Resolving continuous flexibility and discrete heterogeneity from single particle cryo-EM. J. Struct. Biol. *213*, 107702.
41. Punjani, A., Zhang, H., and Fleet, D.J. (2020). Non-uniform refinement: adaptive regularization improves single-particle cryo-EM reconstruction. Nat. Methods *17*, 1214–1221.
42. Punjani, A., Rubinstein, J.L., Fleet, D.J., and Brubaker, M.A. (2017). cryoSPARC: algorithms for rapid unsupervised cryo-EM structure determination. Nat. Methods *14*, 290–296.
43. Emsley, P., and Cowtan, K. (2004). Coot: model-building tools for molecular graphics. Acta Crystallogr. D Biol. Crystallogr. *60*, 2126–2132.
44. Croll, T.I. (2018). ISOLDE: a physically realistic environment for model building into low-resolution electron-density maps. Acta Crystallogr. D Struct. Biol. *74*, 519–530.
45. Moriarty, N.W., Grosse-Kunstleve, R.W., and Adams, P.D. (2009). electronic Ligand Builder and Optimization Workbench (eLBOW): a tool for ligand coordinate and restraint generation. Acta Crystallogr. D Biol. Crystallogr. *65*, 1074–1080.
46. Adams, P.D., Grosse-Kunstleve, R.W., Hung, L.W., Ioerger, T.R., McCoy, A.J., Moriarty, N.W., Read, R.J., Sacchettini, J.C., Sauter, N.K., and Terwilliger, T.C. (2002). PHENIX: building new software for automated crystallographic structure determination. Acta Crystallogr. D Biol. Crystallogr. *58*, 1948–1954.
47. Smart, O.S., Neduvelil, J.G., Wang, X., Wallace, B.A., and Sansom, M.S. (1996). HOLE: a program for the analysis of the pore dimensions of ion channel structural models. J. Mol. Graph. *14*, 354–360. 376.
48. Laskowski, R.A., and Swindells, M.B. (2011). LigPlot+: multiple ligand-protein interaction diagrams for drug discovery. J. Chem. Inf. Model. *51*, 2778–2786.
49. Jo, S., Kim, T., Iyer, V.G., and Im, W. (2008). CHARMM-GUI: a web-based graphical user interface for CHARMM. J. Comput. Chem. *29*, 1859–1865.
50. Jorgensen, W.L., Chandrasekhar, J., Madura, J.D., Impey, R.W., and Klein, M.L. (1983). Comparison of simple potential functions for simulating liquid water. J. Chem. Phys. *79*, 926–935.
51. Yu, W., He, X., Vanommeslaeghe, K., and MacKerell, A.D., Jr. (2012). Extension of the CHARMM General Force Field to sulfonyl-containing compounds and its utility in biomolecular simulations. J. Comput. Chem. *33*, 2451–2468.
52. Vanommeslaeghe, K., Hatcher, E., Acharya, C., Kundu, S., Zhong, S., Shim, J., Darian, E., Guvench, O., Lopes, P., Vorobyov, I., and Mackerell, A.D., Jr. (2010). CHARMM general force field: A force field for drug-like molecules compatible with the CHARMM all-atom additive biological force fields. J. Comput. Chem. *31*, 671–690.
53. Berendsen, H.J.C., van der Spoel, D., and van Drunen, R. (1995). GROMACS: A message-passing parallel molecular dynamics implementation. Comput. Phys. Commun. *91*, 43–56.
54. Klauda, J.B., Venable, R.M., Freites, J.A., O'Connor, J.W., Tobias, D.J., Mondragon-Ramirez, C., Vorobyov, I., MacKerell, A.D., Jr., and Pastor, R.W. (2010). Update of the CHARMM all-atom additive force field for lipids: validation on six lipid types. J. Phys. Chem. B *114*, 7830–7843.
55. Parrinello, M., and Rahman, A. (1981). Polymorphic transitions in single crystals: A new molecular dynamics method. J. Appl. Phys. *52*, 7182–7190.
56. Darden, T., York, D., and Pedersen, L. (1993). Particle mesh Ewald: An*N*·log(*N*) method for Ewald sums in large systems. J. Chem. Phys. *98*, 10089–10092.
57. Kumari, R., and Kumar, R.; Open Source Drug Discovery Consortium (2014). g_mmpbsa–a GROMACS tool for high-throughput MM-PBSA calculations. J. Chem. Inf. Model. *54*, 1951–1962.
58. Hodges, R.S., Heaton, R.J., Parker, J.M., Molday, L., and Molday, R.S. (1988). Antigen-antibody interaction. Synthetic peptides define linear antigenic determinants recognized by monoclonal antibodies directed to the cytoplasmic carboxyl terminus of rhodopsin. J. Biol. Chem. *263*, 11768–11775.
59. Pettersen, E.F., Goddard, T.D., Huang, C.C., Couch, G.S., Greenblatt, D.M., Meng, E.C., and Ferrin, T.E. (2004). UCSF Chimera–a visualization system for exploratory research and analysis. J. Comput. Chem. *25*, 1605–1612.

60. Goddard, T.D., Huang, C.C., Meng, E.C., Pettersen, E.F., Couch, G.S., Morris, J.H., and Ferrin, T.E. (2018). UCSF ChimeraX: Meeting modern challenges in visualization and analysis. Protein Sci. *27*, 14–25.

61. Pettersen, E.F., Goddard, T.D., Huang, C.C., Meng, E.C., Couch, G.S., Croll, T.I., Morris, J.H., and Ferrin, T.E. (2021). UCSF ChimeraX: Structure visualization for researchers, educators, and developers. Protein Sci. *30*, 70–82.

62. Lomize, A.L., Todd, S.C., and Pogozheva, I.D. (2022). Spatial arrangement of proteins in planar and curved membranes by PPM 3.0. Protein Sci. *31*, 209–220.

63. Humphrey, W., Dalke, A., and Schulten, K. (1996). VMD: visual molecular dynamics. J. Mol. Graph. *14*, 33–38. 27-28.

64. Wickham, H., and Sievert, C. (2016). ggplot2: Elegant Graphics for Data Analysis, Second edition (New York: Springer-Verlag).

STAR★METHODS

KEY RESOURCES TABLE

REAGENT or RESOURCE	SOURCE	IDENTIFIER
Antibodies		
1D4 primary antibody	Hodges et al.[58]	N/A
Chemicals, peptides, and recombinant proteins		
SD-Leu Media	Fisher BoiReagents	Cat# MP114811075
Glycerol	Fisher BioReagents	Cat# BP229-4
Protease inhibitor cocktail	Sigma-Aldrich	Cat# P8215
CnBr-activated Sepharose beads	Cytiva	Cat# 17043001
1D4 peptide	Genscript	N/A
Lauryl Maltose Neopentyl Glycol (LMNG)	Anatrace	Cat# NG310
Decyl Maltose Neopentyl Glycol (DMNG)	Anatrace	Cat# NG322
TCEP	Pierce	Cat# PG82090
Soy polar lipids	Avanti	Cat# 541602C
MSP2N2	Grinkova et al.[39] Addgene	Cat# 29520
Bio-Beads SM-2 Absorbent media	BioRad	Cat# 1528920
diC8-PI(4,5)P_2	Echelon Biosciences	Cat# P-4508
Econazole nitrate	Cayman	Cat #20223
Econazole nitrate	Thermo Scientific Chemicals	Cat# J63173.06
Effectene Transfection Reagent	Qiagen	Cat# 301425
Poly-L-lysine	Sigma-Aldrich	Cat# P4707
Critical commercial assays		
Alkali-Cation Yeast Transformation Kit	MP Biomedicals	Cat# 112200200
QuikChange II XL Site Directed Mutagenesis Kit	Agilent	Cat# 200522
Deposited data		
$TRPV5_{ECN}$	This paper	PDB: 8TF3; EMDB: 41218
$TRPV5_{PIP2+ECN}$	This paper	PDB: 8TF4; EMDB: 41219
$TRPV5_{Apo}$	This paper	PDB: 8TF2; EMDB: 41217
$TRPV5_{Apo,\ pH8}$	Fluck et al.[15]	PDB: 7T6J; EMDB: 25716
$TRPV6_{ECN}$	Neuberger et al.[29]	PDB: 7S8C; EMDB: 24893
$TRPV5_{PIP2}$	Lee et al.[30]	PDB: 8FFO; EMDB: 29049
Experimental models: Cell lines		
Human Embryonic Kidney 293 (HEK293) cells	ATCC	Cat# CRL-1573
Experimental Models: Organisms/Strains		
Saccharomyces cerevisiae BJ5457	ATCC	Cat# 208282
Oligonucleotides		
TRPV5 F472A Forward primer: ATGGGCCTAGCATCT GGGCTCCTCGAGCAAAGTACATG	Eton Bioscience	N/A
TRPV5 F472A Reversed primer: CATGTACTTTGCTCG AGGAGCCCAGATGCTAGGCCCAT	Eton Bioscience	N/A
TRPV5 L475A Forward primer: TGATGGTGAATGGGCC TGCCATCTGGAATCCTCGAG	Eton Bioscience	N/A
TRPV5 L475A Reversed primer: CTCGAGGATTCCAGA TGGCAGGCCCATTCACCATCA	Eton Bioscience	N/A
TRPV5 F472A + L475A Forward primer: ATGGTGAATG GGCCTGCCATCTGGGCTCCTCG	Eton Bioscience	N/A

(*Continued on next page*)

Continued

REAGENT or RESOURCE	SOURCE	IDENTIFIER
TRPV5 F472A + L475A Reversed primer: CGAGGAGC CCAGATGGCAGGCCCATTCACCAT	Eton Bioscience	N/A
TRPV5 W495A Forward primer: GATAACCACAGCCAT TAGCGCGCAGAAACGCATTAGGTCT	Eton Bioscience	N/A
TRPV5 W495A Reversed primer: AGACCTAATGCGTTT CTGCGCGCTAATGGCTGTGGTTATC	Eton Bioscience	N/A
TRPV5 L475E Forward primer: CATGATGGTGAATGGG CCCTCCATCTGGAATCCTCGAGC	Eton Bioscience	N/A
TRPV5 L475E Reversed primer: GCTCGAGGATTCCAG ATGGAGGGCCCATTCACCATCATG	Eton Bioscience	N/A
TRPV5 L475D Forward primer: CATGATGGTGAATGG GCCATCCATCTGGAATCCTCGAGC	Eton Bioscience	N/A
TRPV5 L475D Reversed primer: GCTCGAGGATTCCAG ATGGATGGCCCATTCACCATCATG	Eton Bioscience	N/A
TRPV5 L475K Forward primer: ATGATGGTGAATGGGC CTTTCATCTGGAATCCTCGAGC	Eton Bioscience	N/A
TRPV5 L475K Reversed primer: GCTCGAGGATTCCAG ATGAAAGGCCCATTCACCATCAT	Eton Bioscience	N/A
TRPV5 L475R Forward primer: ATGATGGTGAATGGGC CTCTCATCTGGAATCCTCGAGC	Eton Bioscience	N/A
TRPV5 L475R Reversed primer: GCTCGAGGATTCCAG ATGAGAGGCCCATTCACCATCAT	Eton Bioscience	N/A
Recombinant DNA		
YepM rabbit TRPV5 plasmid	Moiseenkova-Bell et al.[38]	N/A
GCaMP6 plasmid	Hughes et al.[23]	N/A
rabbit TRPV5-IRES-GFP plasmid	Hughes et al.[23]	N/A
Software and algorithms		
pClamp 11.1	Molecular Devices	https://www.moleculardevices.com/products/axon-patch-clamp-system/acquisition-and-analysis-software/pclamp-software-suite
cryoSPARC v4.0.x	Punjani et al.[40] Punjani et al.[41] Punjani et al.[42]	https://cryosparc.com
COOT	Emsley et al.[43]	https://www2.mrc-lmb.cam.ac.uk/personal/pemsley/coot
ISOLDE	Croll et al.[44]	https://tristanic.github.io/isolde/
eLBOW	Moriarty et al.[45]	https://phenix-online.org/documentation/reference/elbow_gui.html
PHENIX	Adams et al.[46]	https://phenix-online.org/documentation/index.html
HOLE	Smart et al.[47]	http://www.holeprogram.org/
Chimera	Pettersen et al.[59]	https://www.cgl.ucsf.edu/chimera/
ChimeraX	Goddard et al.[60] Pettersen et al.[61]	https://www.cgl.ucsf.edu/chimerax/
PyMol 2.3	Schrodinger, Inc.	https://pymol.org/2/
LigPlot	Laskowski and Swindells[48]	https://www.ebi.ac.uk/thornton-srv/software/LigPlus/download.html
CHARMM-GUI	Jo et al.[49]	http://www.charmm-gui.org
Positioning of Proteins in Membrane server	Lomize et al.[62]	http://opm.phar.umich.edu/server.php
CHARMM General Force Field (CGenFF) server	Yu et al.[51] Vanommeslaeghe et al.[52]	https://cgenff.umaryland.edu
Gromacs 2020.2	Berendsen et al.[53]	https://www.gromacs.org/
g_mmpbsa tool	Kumari et al.[57]	https://github.com/RashmiKumari/g_mmpbsa

(*Continued on next page*)

Continued

REAGENT or RESOURCE	SOURCE	IDENTIFIER
VMD	Humphrey et al.[63]	https://www.ks.uiuc.edu/Research/vmd/
Origin 8.5.1	Origin Lab	https://www.originlab.com/
Excel	Microsoft	https://www.microsoft.com/en-us/microsoft-365/excel
ggplot2	Wickham[64]	https://ggplot2.tidyverse.org

RESOURCE AVAILABILITY

Lead contact

Further information and requests for either resources or reagents should be directed to and will be fulfilled by the lead contact, Vera Y. Moiseenkova-Bell (vmb@pennmedicine.upenn.edu).

Materials availability

Requests for materials generated in this study should be directed to and will be fulfilled by the lead contact Vera Y. Moiseenkova-Bell (vmb@pennmedicine.upenn.edu).

Data and code availability

All data generated in these studies are available upon request from lead contact Vera Y. Moiseenkova-Bell (vmb@pennmedicine.upenn.edu). The atomic coordinates and cryo-EM density maps of the structures presented in this paper are deposited in the Protein DataBank and Electron Microscopy DataBank under the accession codes $TRPV5_{ECN}$ (PDB: 8TF3 and EMDB: EMD-41218), $TRPV5_{PIP2+ECN}$ (PDB: 8TF4 and EMDB: EMD-41219), $TRPV5_{Apo}$ (PDB: 8TF2 and EMDB: EMD-41217). This paper does not report original code.

EXPERIMENTAL MODEL AND STUDY PARTICIPANT DETAILS

For structural studies, the TRPV5 channel was expressed in BJ5457 Saccharomyces cerevisiae (ATCC, Cat# 208282) with a YepM plasmid bearing rabbit TRPV5 sequence with 1D4 epitope tag and maintained at 30°C, using an alkali-cation yeast transformation kit (MP Biomedicals, Cat# 112200200) according to the instruction of the manufacturer. For expression of TRPV5 channel in electrophysiological or for intracellular Ca^{2+} measurements studies, Human Embryonic Kidney 293 (HEK293) cells (ATCC, Cat# CRL-1573) were transfected with 200 ng rbTRPV5-IRES-GFP (wild-type or mutant) using the Effectene transfection reagent (Qiagen, Cat# 301425). Additional details can be found in the method details.

METHOD DETAILS

TRPV5 protein preparation

TRPV5 preparation followed the previously established protocol described in Fluck et al., 2021. Briefly, TRPV5 with a C-terminal 1D4 epitope tag in a YepM vector[38] was transfected into BJ5457 *Saccharomyces cerevisiae* (ATCC) using an alkali-cation yeast transformation kit (MP Biomedicals) according to the instruction of the manufacturer. Transformed cells were plated on SD-Leu agar plates and allowed to grow at 30°C for 2 days 30–50 colonies were picked from a plate and inoculated into a single 125 mL starter culture containing SD-Leu media and 10% *v*/v glycerol. The culture was incubated at 30°C until reaching the top of the log phase (OD 1.0–1.4). After confirmation of protein expression by Western blot, the cells were grown at 30°C with shaking at 200 rpm in 2.5 L of media per flask until OD of 1.0–1.4 was reached. Cells were harvested by centrifugation at 3000 × *g*, resuspended in storage buffer (25 mM Tris-HCl, pH 8.0, 300 mM sucrose, and 1 mM PMSF) on ice, and then spun down at 3000 × *g* to discard the supernatant. Cell pellets were subsequently stored at −80°C. This expression culture was propagated using 15 mL of the previous growth at OD 1.0–1.4 for several days until the desired amount was obtained.

Approximately 60 L of growth cells were thawed and resuspended in 300 mL of homogenization buffer (25 mM Tris-HCl, pH 8.0, 300 mM sucrose, 5 mM EDTA, and protease inhibitor cocktail). The resuspended cells were lysed using a M110Y microfluidizer (Microfluidics) at 100–120 psi. The membranes were separated from cellular debris by centrifugation at 3,000 × *g* for 10 min, followed by centrifugation of the supernatant at 14,000 × *g* for 35 min. The membranes obtained from the previous spin were then pelleted at 100,000 × *g* for 1 h. The pelleted membranes were harvested and resuspended on ice using a 15 mL tissue homogenizer (Kontes Duall with PTFE pestle) in buffer containing 25 mM Tris-HCl, pH 8.0, 300 mM sucrose, and 1 mM PMSF, and stored at −80°C.

TRPV5 was solubilized from the thawed membranes in solubilization buffer (20 mM HEPES, pH 8.0, 150 mM NaCl, 2 mM TCEP, and 0.87 mM LMNG). The insoluble fraction was separated by centrifugation at 100,000 × *g* for 1 h. The resulting supernatant was incubated with 1D4-antibody coupled to CnBr-activated Sepharose beads for 3 h. The beads were collected on a gravity flow column, washed with wash buffer (20 mM HEPES, pH 8.0, 150 mM NaCl, 2 mM TCEP, and 0.064 mM DMNG). The beads were incubated with

elution buffer (20 mM HEPES, pH 8.0, 150 mM NaCl, 2 mM TCEP, and 0.064 mM DMNG, 3 mg/mL 1D4 peptide) overnight. TRPV5 was eluted in 1 mL fractions every 5 min. Peak fractions were pooled and concentrated using a 100-kDa concentrator (Millipore). For reconstitution into nanodiscs, an equimolar amount of MSP2N2 protein[39] was incubated with the detergent-solubilized TRPV5 in the presence of soy polar lipids and DMNG detergent in a 1 mL reaction volume. The ratio of TRPV5:MSP2N2:lipid:DMNG in mixture was 1:1:200:500. The reaction mixture was incubated on ice for 30 min, followed by the addition of ~30 μL of Bio-Beads. The mixture was rotated at 4°C for 1 h. The supernatant was transferred to a new tube, and another 30 μL of fresh Bio-Beads was added before rotating at 4°C overnight to complete the reaction. Reconstituted TRPV5 was subjected to a Superose 6 increase 10/300 GL column (GE Healthcare) equilibrated with 20 mM HEPES, pH 8.0, 150 mM NaCl, 2 mM TCEP (SEC buffer). Fractions containing nanodisc reconstituted TRPV5 were pooled and concentrated to 2.15 mg/mL.

Cryo-EM sample preparation and data collection

$TRPV5_{ECN}$ and $TRPV5_{PIP2+ECN}$ samples were incubated with 500 μM econazole or with 500 μM + 400 μM diC8-PI(4,5)P_2 (Echelon Biosciences) for 45 min, respectively. Econazole was solubilized in 100% DMSO (100 mM) and then diluted at 15% in SEC buffer (15 mM). $TRPV5_{Apo}$ sample was blotted after concentration without any treatment. Using a Vitrobot Mark IV (Thermo Scientific), 3 μL of the samples were applied to glow-discharged 1.2/1.3 Quantifoil Holey Carbon Grids (Quantifoil Micro Tools). The sample was blotted in a chamber at 4°C and 100% humidity for 6 s at 0 blotting force before being freezing in liquid ethane.

Samples were imaged on a Titan Krios G3i 300 kV electron microscope with a Gatan K3 direct electron detector. 35–42 frame movies were collected with a nominal dose of 41–42 $e^-/Å^2$. Super-resolution images for all datasets were collected at 105,000 magnification with a pixel size of 0.415 Å/pixel.

Data processing

Two datasets of 4,757 (DS1) and 6,589 (DS2) movies were collected for the $TRPV5_{PIP2+ECN}$, and processed in cryoSPARC v4.0.1.[40–42] Movies were patch motion corrected with a Fourier crop factor of 0.5 and an alignment resolution of 4 Å, and then the patch CTF was estimated. The template for autopicking was created with 99,610 (DS1) and 94,010 (DS2) particles blob picked from subsets of 300 micrographs and used for extraction. 676,422 and 639,819 particles were extracted and binned by a factor of 4 with a box size of 72 pixels from DS1 and DS2, respectively. These particles were 2D classified with 100 classes, resulting in 126,429 (DS1) and 180,083 (DS2) good particles that were re-extracted. Particles were oriented with the TRPV5 apo map (EMD-25716) and refined with a non-uniform refinement in C1 and C4 symmetry to generate the initial model.[41] A three-class heterogeneous refinement was performed to separate good particles, resulting in a good class of 86,585 (DS1) and 123,813 (DS2) particles at 1.66 Å/pix. Particles from DS1 were subjected to 3D classification with 5 classes focusing on the pore region. The best three classes, totaling 47,825 particles, were combined to produce a final structure with a resolution of 3.4 Å in C4 symmetry at 0.83 Å/pix. On the other hand, particles from DS2 were subjected to 3D variability focused on the pore with 10 frames. The best frames were combined, resulting in 70,638 particles and a final structure with a resolution of 3.10 Å in C4 symmetry at 0.83 Å/pix. The final model from both datasets was combined and heterogenously refined into three volumes. The best structure form with 101.063 particles was refined with a non-uniform refinement to produce the final maps in C1 and C4 symmetry at a resolution of 3.18 Å and 2.86 Å, respectively.

For $TRPV5_{ECN}$ datasets, 6,018 movies were collected and processed using cryoSPARC v4.0.2.[40–42] Movies were patch motion corrected with an alignment resolution of 4 Å and a Fourier crop factor of 0.5, and then run through patch CTF estimation. Images were then autopicked using 2D templates generated from a subset of 300 micrographs. 1,426,748 million of particles were extracted and sorted by 2D classification into 100 classes at 3.32 Å/pix. The remaining 324,769 particles were re-extracted at 1.66 Å/pix to generate the first model using non-uniform (NU) refinement with the TRPV5 Apo (EMD-25716) as a reference model. These particles were heterogeneously refined into 3 classes. The 200,376 particles from the best class were re-extracted at 0.83 Å/pix, and NU refined in C1 symmetry; then subjected to another round of heterogeneous refinement into 4 classes. Two classes consisting of 173,323 particles were combined to produce the final maps in C1 and C4 symmetry at resolutions of 3.25 Å and 2.94 Å, respectively.

Similarly, for $TRPV5_{Apo}$ datasets 6,049 movies were collected and processed on cryoSPARC v4.0.2.[40–42] Movies were patch motion corrected with an alignment resolution of 4 Å and a Fourier crop factor of 0.5, then the patch CTF was estimated. 2,300,807 million of particles were autopicked, extracted and sorted with 2D classification into 100 classes at 3.32 Å/pix The template for 2D autopick was built from a subset of 300 micrographs. 704,782 were selected and heterogeneously refined into 3 classes. The best class of 439,479 particles was re-extracted at 1.66 Å/pix and subjected to another round of heterogeneous refinement into 3 classes. The best class were re-extracted at 0.83 Å/pix and NU refined in C4 symmetry (2.93 Å), then subjected to 3D classification into 3 classes focused on the pore. The best map forming with 79,632 particles was NU refined to generate the final map with a resolution of 2.57 Å in C4 symmetry.

The local resolution of all structures was determined in cryoSPARC, and the angular distributions were generated with the UCSF pyem package.

Model building

The TRPV5 apo state model (7T6J)[15] was used as the initial model for each structure, and manually adjusted in COOT[43] and ISOLDE,[44] then lipids, PI(4,5)P_2, and econazole, obtained from the ePDB database, were docked and manually adjusted. Real Space_Refinement and eLBOW[45] from the PHENIX software[46] were used to refine and to generate ligand restraints, respectively.

Pore profiles were determined using HOLE.[47] Chimera, ChimeraX, and PyMol were used for analysis, visualization and figure generation. LigPlot+[48] was used to determine molecular contacts.

Molecular dynamics simulations

The $TRPV5_{PIP2+ECN}$ coordinate model, oriented using the 6DMU model from the Positioning of Proteins in Membrane server(http://opm.phar.umich.edu/server.php), was embedded in a 1-palmitoyl-2-oleoyl-*sn*-glycerol-3-phosphocholine (POPC) lipid bilayer with phosphatidylinositol-4-5-bisphosphate, modeled with SAPI2, and ergosterol, built in the CHARMM-GUI[49] membrane builder(http://www.charmm-gui.org). The protein-membrane complex was solvated with water modeled by TIP3,[50] and 100 mM $CaCl_2$. The MD simulation system consists of 569 POPC, 25 ERG, 22 PIP2, 93166 TIP3, 234 Ca^{2+}, 340 Cl^-, and 4 ECN molecules contained them in a 163 × 163 × 163 $Å^3$ simulation box. The force field parameters for R-econazole (1-[(2R)-2-[(4-chlorobenzyl)oxy]-2-(2,4-dichlorophenyl)ethyl]-1H-imidazole) were generated using the CHARMM General Force Field (CGenFF) server(https://cgenff.umaryland.edu).[51,52] The four econazole molecules were placed at the determined position in the $TRPV5_{PIP2+ECL}$ structure.

MD simulations were performed using the GPU-accelerated Gromacs 2020.2 package[53] with the CHARMM36 force field.[54] The ensemble was minimized and equilibrated using the six steep descent algorithm of the CHARMM GUI. The temperature was maintained at 303 K and the pressure at 1 bar using a Nosé–Hoover thermostat and the Parrinello–Rahman barostat,[55] respectively. Bond distances were kept rigid by using the LINCS algorithm. The Particle Mesh Ewald (PME) algorithm was used to calculate long-range electrostatic interactions every 2 fs with a cutoff of 12 Å.[56] The van der Waals interactions were switched at 10 Å and cutoff at 12 Å. Data were collected from 5 rounds of 500 ns simulation each.

Free energies of binding were calculated every 10 ns for each simulation using the g_mmpbsa tool and the solvent accessible surface area (SASA) model.[57]

MD simulations were analyzed using Gromacs tools and VMD.

Whole-cell patch clamp

Human Embryonic Kidney 293 (HEK293) cells (ATCC, Cat.: CRL-1573) were transfected with 200 ng rbTRPV5-IRES-GFP (wild-type or mutant) using the Effectene transfection reagent (Qiagen). Cells were plated on poly-L-lysine (Sigma, Cat.: P4707) coated 12 mm glass coverslips 24 h after transfection, and patch clamp experiments were performed 48 h after transfection. Whole-cell patch-clamp recordings were carried out using an Axopatch 200B amplifier (Molecular Devices), a Digidata 1440 unit (Molecular Devices), and pClamp 11.1. Patch pipettes were prepared using a P-97 puller (Sutter Instruments) from borosilicate glass capillaries (Sutter Instruments) with a resistance in the range of 2–5 MΩ. After establishing a GΩ seal, a brief negative pressure was applied to establish a whole-cell configuration. A voltage ramp from −100 mV to +100 mV was applied every second during recording, and currents were filtered at 2 kHz with a low-pass Bessel filter. Cells were maintained in a lithium-based extracellular solution (142 mM LiCl, 1 mM $MgCl_2$, 10 mM HEPES, and 10 mM glucose; pH adjusted to 7.4 with LiOH), and monovalent currents were elicited by application a Mg^{2+}-free solution (142 mM LiCl, 1 mM EGTA, 10 mM HEPES, and 10 mM glucose; pH adjusted to 7.4 with LiOH). The charge carrier for inward currents in this solution is Li^+, as it minimizes background currents in the divalent free solution.[23,24] Patch pipettes were filled with an intracellular solution containing 140 mM K-Gluconate, 2 mM $MgCl_2$, 2 mM Na_2ATP, 5 mM EGTA, and 10 mM HEPES (pH adjusted to 7.3 with KOH). Once TRPV5 currents stabilized, 10 μM econazole nitrate (Cayman Chemical Company, Cat.: 20223) was perfused for 2 min. Currents were analyzed with Clampfit 11.1. All experiments were performed at room temperature (22°C–24°C).

Intracellular Ca^{2+} measurements

HEK293 cells were co-transfected with wild-type rbTRPV5, L475A, or F472A DNA with GCaMP6 using Effectene transfection reagent (Qiagen). After 24 h, the transfected cells were plated in a poly-L-lysine coated black-wall clear bottom 96 well plate. Measurements were performed 48 h after plating. Thirty minutes before the experiment, the serum containing MEM media on the cells was replaced with a Ca^{2+} free solution containing 137 mM NaCl, 5 mM KCl, 1 mM $MgCl_2$, 10 mM HEPES, and 10 mM glucose, pH7.4. Intracellular calcium levels were measured by GCaMP6 signals at excitation wavelengths 485 nm and emission detected at 525 nm using the Flexstation-3 plate reader (Molecular Devices). Various concentrations of econazole were applied prior to the application of 1 mM Ca^{2+} to induce Ca^{2+} influx through TRPV5. Background Ca^{2+} influx was also recorded in cells transfected with GCaMP only (Figure S4D) Econazole nitrate (Cayman, Cat.: 20223) was dissolved in DMSO as a 50 mM stock solution. The stock was further diluted with experimental buffer. Due to solubility limitations, 30 μM was the highest concentration used. Three separate transfections were performed for each group, and the signals from three replicates of each transfection were averaged and treated as one data point for data plotting.

QUANTIFICATION AND STATISTICAL ANALYSIS

Cryo-EM data were processed using cryoSPARC v4.0.x.[40–42] Statistical significance was calculated using one-way analysis of variance and Tukey's post hoc test using Origin 8.5.1 (Origin Lab). Mean dose-responses were determined using three replicates (n = 3) from each transfection. $TRPV5_{PIP2+ECN}$, $TRPV5_{ECN}$ RMSD with respect to $TRPV5_{Apo}$ were calculated using PyMol. *rms* and *rmsf* gromacs tools were used to determine RMSD and RMDF, respectively, from the 5 replicas of MD simulation. The distance between the ECN and the binding site were determined using the *mindist* gromacs tool. Excel and ggplot2 package were used for plotting. Statistical details are described in the figure captions. All data plotted as mean ± SEM.